Front. Energy 2025, 19(5): 729–737
https://doi.org/10.1007/s11708-025-1006-4

RESEARCH ARTICLE

An ultra-low platinum loading ORR electrocatalyst with high efficiency: Synergistic effects of Pt and Fe-N-C support

Wenbin Tang[1], Shuyue Xia[1], Haiwen Chou[1], Jianan Zhao[1], Yi Zhou[2], Qinghong Huang (✉)[1], Nengfei Yu[1], Yuping Wu[1]

1 Nanjing Tech University, Nanjing 211816, China
2 Jiangsu Industrial Technology Research Institute, Nanjing 211800, China

Abstract The oxygen reduction reaction (ORR) plays a crucial role in key processes of fuel cells and zinc-air batteries. To enable commercialization, reducing the platinum (Pt) content and increasing the specific activity per unit mass is essential. A promising approach involves synthesizing of Fe-N-C precursors via the polyaniline (PANI) pathway, which ensures a uniform distribution of Fe-N-C species and facilitates the subsequent adsorption of platinum ions. This leads to the formation of Pt-Fe bimetallic alloys. The synergistic interaction between Pt and Fe-N-C sites promotes the homogeneous dispersion of Pt and the formation of smaller particle sizes, which in turn enhances intrinsic activity and stability of the catalyst. Notably, the Pt/Fe-N-C catalyst, featuring an ultra-low Pt loading of just 1.79 wt%, exhibits a remarkable doubling of mass activity compared to conventional catalysts. Moreover, zinc-air batteries using this catalyst achieve an impressive peak power density of 200 mW/cm^2.

Keywords oxygen reduction reaction (ORR), fuel cells, Pt-Fe-N-C catalysts, synergistic effect, mass activity

1 Introduction

The relentless exploitation of conventional fossil fuels, coupled with the growing concern over environmental pollution, has significantly accelerated the development of efficient, clean, and renewable energy devices such as fuel cells, supercapacitors, lithium-ion batteries, hydroelectrolysis and zinc-air batteries [1–5]. Among these technologies, zinc-air batteries and fuel cells have great potential for development in future energy systems because of their high energy density and inherent environmental sustainability [6–8]. These devices provide stable power output under normal conditions, making them ideal for low-power electronic devices. Nevertheless, the relatively slow kinetics of the electrochemical oxygen reduction reaction (ORR) at the cathode remains a major challenge, hindering the widespread commercialization of these energy devices.

Platinum-based noble metal catalysts have the best performance and stability for ORR. However, issues such as platinum's high cost, limited availability, and poor cycling stability have severely hindered its commercialization [9,10]. Consequently, developing cost-effective, high-performance, low-platinum catalysts has become a key strategy for improving ORR activity [11,12]. Low-platinum loading catalysts meet demand by reducing platinum usage and cost while maintaining or enhancing the catalyst activity and stability. Research on low-platinum loading catalysts includes platinum-based alloys, platinum-based core-shell structures, and platinum single-atom catalysts (SACs) [13,14]. Platinum-based alloy catalysts, such as platinum-nickel, platinum-iron, platinum-cobalt have significant advantages in catalytic activity, stability, and reduced precious metal usage. Transition metals enhance platinum's catalytic activity by optimizing its surface electronic structures, making these alloys increasingly important for ORR research and applications [15,16]. Zhang et al. provided a comprehensive review of the design concepts and synthesis methods of various alloyed and nanoparticle-containing SACs, which offered valuable insights for this study [17–19].

Despite advancements, there are still areas for improvement in platinum-based alloy catalysts. First, the high cost and relatively high platinum usage pose

Received Jan. 15, 2025; accepted Mar. 24, 2025; online May 1, 2025
Correspondence: Qinghong Huang, huangqh@njtech.edu.cn

significant challenges. For example, commercially produced platinum alloy catalysts in mass-produced fuel cells typically have platinum content of around 10%. Next, the synthesis process is complex, and large-scale production is not feasible due to laboratory-scale limitations. Finally, the weak interfacial interaction between the support and the metal component can lead to metal particle detachment and aggregation, reducing in activity [20–22].

Polyaniline (PANI) is a cost-effective and easy-to-synthesize material with remarkable electrical conductivity. It can be fabricated into various nanostructures such as nanospheres, nanorods, nanosheets, and nanofibers. Furthermore, the introduction of porous structures enhances its properties, and functional groups can be tailored to suit specific applications [23–27]. As a precursor, PANI offers several advantages including enhanced catalyst performance due to its conductive properties and structural flexibility. Upon undergoing thermal treatment, PANI can be converted into carbon-based materials while maintaining metal dispersion and catalytic efficacy [28,29].

In this study, the Fe-N-C precursor was prepared via the PANI pathway. The dispersion and exposure of Fe-N-C sites were enhanced by employing Lewis doping theory and the self-structural constraint effect. The PANI structure consists of oxidized quinone units (QI) and reduced benzene units (BA). Protonic acid doping occurs on the nitrogen atom of QI, which leads to the incorporation of protons into the polymer chain, making it positively charged. To maintain electrical neutrality, corresponding anions enter the polymer chain. The protic acid-doped PANI is then treated with dilute ammonia to form emeraldine base PANI, which, as a transition metal cation of Lewis acid can coordinate with transition cations, forming a PANI-transition metal complex [30]. By adjusting the molar ratio of ammonium persulfate (APS) to aniline monomer (AN) or using electrochemical methods, the proportion of QI can be controlled. The elevated formation energy of the BA unit is utilized to effectively inhibit metal agglomeration during thermal treatment, resulting in a uniformly distributed Fe-N-C catalyst support. Subsequently, platinum ions are adsorbed onto the Fe-N-C structure, and thermal treatment forms Pt–Fe bimetallic alloys. The platinum is evenly distributed across the surface, strongly interacting with the support, which significantly mitigates platinum agglomeration and enhances ORR performance [31–33].

While the performance of Pt-based alloy catalyst has been improved, Pt loading has not been sufficiently reduced. For example, the Pt–Co catalyst synthesized by Liu et al. has a Pt loading of 18 wt%, and the Pt of the Pt–Pd catalyst synthesized by Wang et al. also accounts for 10% [34,35]. The synergistic effect in Pt–Fe alloy catalysts is primarily achieved through electronic interactions that optimize platinum's surface electronic structure [36]. In this study, the synergistic effect is not only due to electron transfer from Fe to Pt, which enhances the reaction rate, but also the unique structural and chemical properties of Fe-N-C sites that promote the uniform adsorption and dispersion of Pt ions. The synergistic effect optimizes the reaction pathway, lowers the reaction energy barrier, and further enhances the catalyst's intrinsic activity and stability.

In this study, the use of PANI precursor route and Fe-N-C sites enabled an ultralow Pt loading of 1.79 wt% with high dispersion. Although the catalytic activity and stability are slightly lower than those of the catalyst reported by Hu et al. [37], which had a half-wave potential ($E_{1/2}$) of 0.925 V and only a 4.3% decline in mass activity after 30000 cycles of ADT, the catalyst demonstrates significant cost advantages for practical applications. The Pt/Fe-N-C with a Pt loading of only 1.79 wt% exhibits a mass activity several times higher than Pt/C, and it also exhibits better half-wave potential and durability in acid-base environments. In addition, the Pt–Fe alloy catalyst also shows superior peak power density compared to the Pt/C catalyst in zinc-air battery testing.

2 Experimental

2.1 Chemicals

Aniline (99.5%), ammonium persulfate ($(NH_4)_2S_2O_8$, 99.99%), perchloric acid ($HClO_4$, 37 wt%), platinum tetrachloride ($PtCl_4$, Pt ⩾ 37.5 wt%), iron(II) chloride tetrahydrate ($FeCl_2{\cdot}4H_2O$, 99.995%), and acetonitrile were purchased from Aladdin. The 20 wt% Pt/C catalyst was obtained from Johnson Matthey, and the 5 wt% Nafion solution was sourced from KeMu. Aniline was used after vacuum distillation.

2.2 Synthesis of materials

2.2.1 Synthesis of PANI

PANI was nanorod-shaped and synthesized without a template. First, 1.8 mL aniline was dissolved in 100 mL of 1 mol/L perchloric acid solution and placed in Beaker A. In Beaker B, 4.5 g of APS was dissolved in 100 mL of 1 mol/L perchloric acid solution. The solutions were then subjected to ultrasonic stirring to ensure thorough mixing and pre-cooled at low temperature for 2 h. After cooling, the solutions in Beakers A and B were combined, and the polymerization reaction was allowed to proceed for 24 h. The resulting mixture was then washed multiple times with deionized water and dried overnight to yield emeraldine-salt polyaniline (ES-PANI). The powder was subsequently treated with 1 mol/L aqueous ammonia for

deprotonation, followed by further drying to yield the deprotonated dark blue product, EB-PANI.

2.2.2 Preparation of Pt/Fe-N-C catalyst

Initially, ES-PANI was immersed in 1 mol/L $NH_3 \cdot H_2O$ for 12 h, followed by filtration and drying in a vacuum oven at 80 °C for 12 h to prepare deprotonated polyaniline (EB-PANI) [38–40]. A total of 200 mg of EB-PANI and 0.15 mmol of $FeCl_2 \cdot 4H_2O$ were dissolved in 80 mL of anhydrous acetonitrile, subjected to ultrasonic treatment for 30 min, and stirred at room temperature for 12 h. The mixture was then filtered, thoroughly rinsed, and dried in a vacuum oven at 80 °C for 12 h. After retrieving the sample, the obtained Fe@EB-PANI was carbonized in a tubular furnace under an N_2/H_2 atmosphere with a heating rate of 5 °C/min, reaching 950 °C for 3 h to obtain Fe-N-C. The carbonized sample was then stirred in a 0.5 mol/L H_2SO_4 solution at 80 °C for 12 h for acid leaching, followed by multiple washings and filtration, and finally dried and weighed. A certain amount of $PtCl_4$ (4% relative to the Pt mass) was added to the sample, mixed with deionized water, and then filtered and dried. The resulting mixture was further treated in the tubular furnace at 300 °C for 1 h at a rate of 5 °C/min under an N_2/H_2 atmosphere to obtain the final Pt/Fe-N-C catalyst sample.

2.2.3 Ink preparation of Pt/Fe-N-C catalyst

The catalyst (10 mg) was combined with 1000 μL of isopropanol and 1800 μL of deionized water. To this mixture, 200 μL of a 5% Nafion solution was added as a binder. The resulting ink was prepared for rotating disk electrode (RDE) testing and zinc-air battery applications. The mixture was sonicated for two hours to achieve a homogeneously dispersed catalyst ink solution. After sonication, 9 μL of catalyst ink was carefully pipetted and applied in three aliquots onto the polished and cleaned surface of a glassy carbon electrode. Once applied, the solution was allowed to dry naturally, resulting in a uniform and complete coverage of the electrode surface with the catalyst.

2.2.4 Preparation of zinc-air battery

A zinc plate was used as anode, polished with sandpaper before use. The Pt/Fe-N-C catalyst ink solution was uniformly coated onto the hydrophobic carbon cloth to serve as the cathode, with a loading of 0.5 mg/cm^2. Nickel mesh was used as the current collector, and a 6 mol/L KOH + 0.2 mol/L $ZnCl_2$ solution was used as the electrolyte. The assembly was tested in a zinc-air battery mold with a dimension of 6 cm × 6 cm × 7 cm.

3 Results and discussion

3.1 Physical characterization of Pt/Fe-N-C catalysts

Figure 1 illustrates the preparation process of the Pt/Fe-N-C catalyst. Initially, a uniform Fe-N-C site is formed on the surface of PANI, followed by the pyrothermally adsorption of Pt ions, resulting in a uniform dispersion of Pt/Fe-N-C catalyst.

As shown in the scanning electron microscopy (SEM) (Fig. 2(a)), Pt/Fe-N-C exhibits a nanorod structure with diameters ranging from 40 to 70 nm. Transmission electron microscopy (TEM) images (Figs. 2(b) and S1) reveal the microstructure of the sample, with clear lattice fringes of Pt and a lattice spacing of 0.222 nm, corresponding to the (1 1 1) crystal plane of Pt. Energy dispersive X-ray spectroscopy (EDS) spectra of the Pt/Fe-N-C catalysts conform that C, N, Fe, and Pt atoms are evenly distributed throughout the material (Figs. 2(c)–2(f)).

The crystal phase structure of Pt-based nanoparticles was further investigated utilizing X-ray diffraction (XRD) (Fig. 3(a)). In the XRD spectrum of Pt/Fe-N-C, the wide peak at 26° corresponds to the (0 0 2) crystal

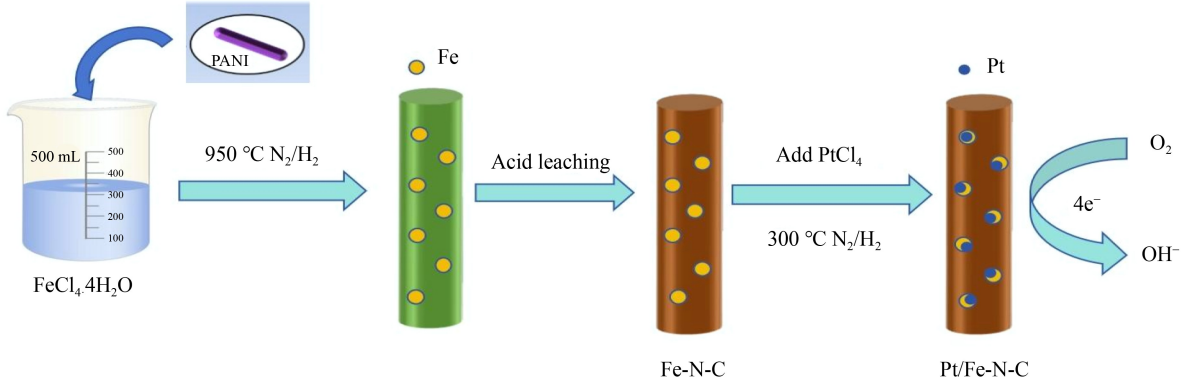

Fig. 1 Schematic diagram illustrating the synthesis process of the Pt/Fe-N-C catalyst.

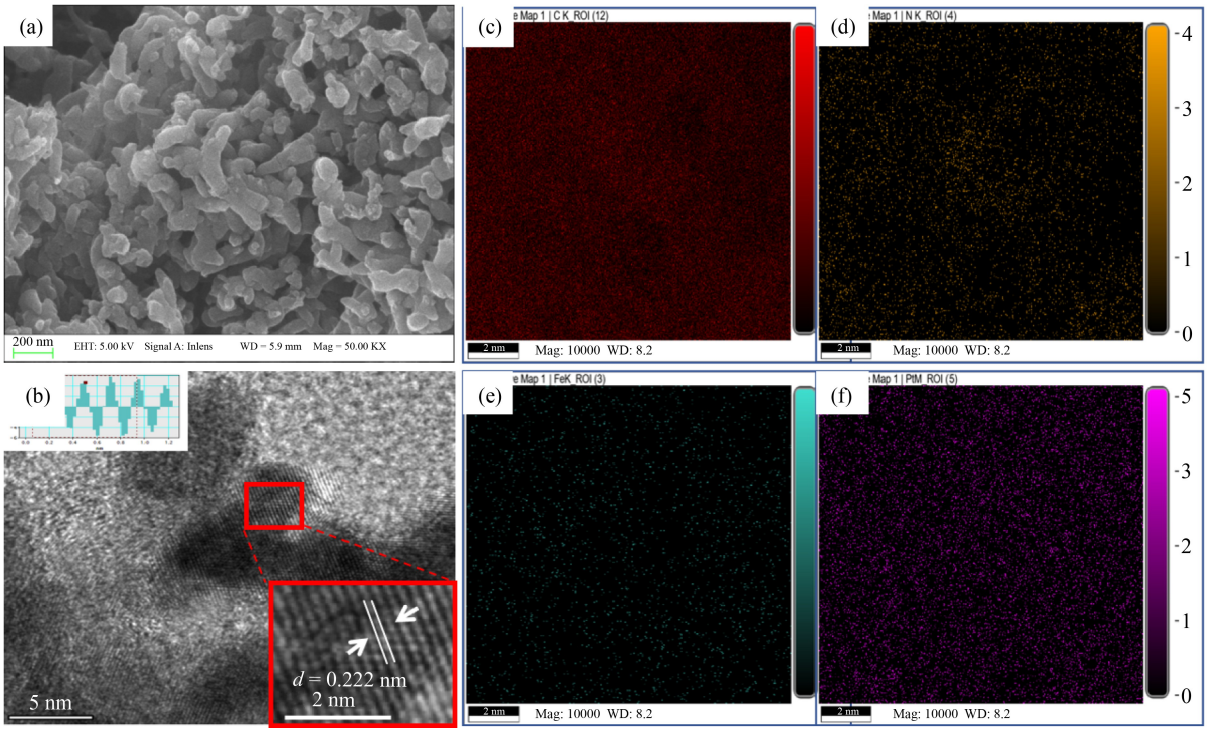

Fig. 2 SEM and TEM images of Pt/Fe-N-C catalyst.
(a) SEM image of Pt/Fe-N-C catalyst 200 nm; (b) TEM images of Pt/Fe-N-C catalyst; (c–f) EDS mapping (C, N, Fe, Pt).

face of graphite, while the diffraction peaks at 40.4°, 47.0°, 69.0°, and 81.2° are attributed to the Pt (1 1 1), (2 0 0), (2 2 0), and (3 1 1) crystal planes, respectively. As shown in Supporting Information Fig. S2, increasing the N_2/H_2 reduction temperature enhances the Pt diffraction peaks and improves the crystallinity. When the heat treatment temperature is raised from 300 to 400 °C, the diffraction peak position remains unchanged, but the peak intensity increases, along with a corresponding increase in particle size.

To accurately determine the Pt and Fe content in the catalyst, inductively coupled plasma (ICP) analysis was performed. In the Pt/Fe-N-C sample, Fe content is 0.64 wt%, and Pt content is 1.79 wt% (Fig. 3(b)), with an atomic ratio of Pt–Fe of approximately 1:1.2. EDS analysis was also conducted to compare the elemental contents, with minimal differences observed. Detailed data is provided in Table S1.

To evaluate the porosity of the Pt/Fe-N-C catalyst, an N_2 adsorption test was performed. As shown in Fig. 3(c), Pt/Fe-N-C has a typical type IV isothermal adsorption curve, with a specific surface area of 230.46 m^2/g.

The elemental composition of the Pt/Fe-N reveals the presence of C, N, O, Pt, and Fe elements. Figures S3(b) and S3(c) show the XPS spectra of C 1s and N 1s for Pt/Fe-N-C. The C 1s spectrum is deconvoluted into two peaks at ~284.6 and ~286.1 eV, corresponding to C−C and C−N bonds, respectively. The N 1s spectrum shows three peaks at 398.4, 400.98, and 402.58 eV, which can be assigned to pyridine nitrogen, graphite nitrogen, and N−O oxide, respectively. Pyridine N is responsible for the formation of Fe-N sites, while graphitic nitrogen promotes the ORR process in the 4-electron pathway [41–44].

The Pt XPS spectrum of Pt/Fe-N-C catalyst is depicted in Fig. 3(d). The spectrum is divided into Pt^0 $4f_{7/2}$ (72.0 eV), Pt^0 $4f_{5/2}$ (75.1 eV), Pt^{2+} $4f_{7/2}$ (73.6 eV), and Pt^{2+} $4f_{5/2}$ (76.6 eV), with the majority of Pt present in the zero-valence state. For the Pt/C catalyst, the spectrum is divided into Pt^0 $4f_{7/2}$ (70.99 eV), Pt^0 $4f_{5/2}$ (74.13 eV), Pt^{2+} $4f_{7/2}$ (72.36 eV), and Pt^{2+} $4f_{5/2}$ (75.09 eV). Both Pt/Fe-N-C and Pt/C show prominent Pt^0 peaks and minor Pt^{2+} peaks with the small presence of Pt^{2+} likely resulting from partial oxidation on the surface of Pt nanoparticles. It is noteworthy that the Pt 4f binding energy for Pt/Fe-N-C exhibits a positive shift of approximately 1.0 eV compared to Pt/C. This positive shift enhances efficient charge transfer, facilitates oxygen molecule capture during the ORR, and consequently promotes more pronounced interfacial charge transfer. The interaction between Pt and Fe induces electron transfer between the metals, modifying their electronic structures, and thereby enhancing the catalyst's functional activity [40].

3.2 Electrocatalytic performances

The performance of the Pt/Fe-N-C catalyst in the ORR was evaluated under both acidic and alkaline conditions.

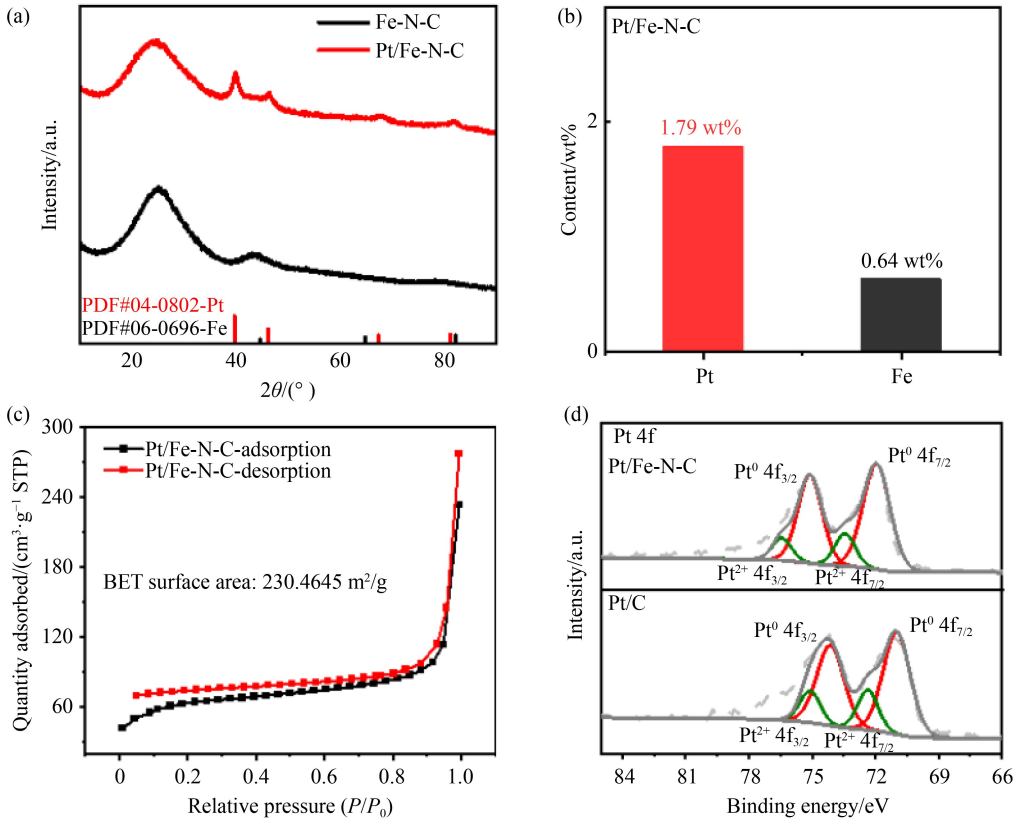

Fig. 3 XRD, ICP, BET, and XPS images of Pt/Fe-N-C catalysts.

(a) XRD curves of the Pt/C and Pt/Fe-N-C; (b) ICP analysis of the Pt/Fe-N-C catalyst revealing the Pt and Fe content; (c) nitrogen adsorption and desorption curve of the Pt/Fe-N-C catalyst; (d) XPS spectra of the Pt/Fe-N-C catalyst and Pt/C catalyst Pt 4f.

The crystallinity of Pt particles is significantly influenced by the temperature and duration of secondary heat treatment. Performance testing under different temperature and time conditions revealed that the catalyst exhibits optimal performance at 300 °C with a treatment time of 1 h (Figs. S4(c) and S4(d)).

In a 0.1 mol/L KOH solution (Fig. 4(a)), the Pt/Fe-N-C catalyst displays a $E_{1/2}$ of 0.85 V, which is significantly higher than that of Pt/C ($E_{1/2}$ = 0.82 V). The accelerated durability test (ADT) of Pt/Fe-N-C and Pt/C was performed for 10000 cycles in a 0.1 mol/L KOH saturated with O_2. Like commercial Pt/C, Pt/Fe-N-C has an $E_{1/2}$ drop of only 20 mV. The kinetic behavior of ORR was analyzed using the Tafel slope, with results indicating that the Tafel slope for Pt/Fe-N-C is 124.89 mV/dec, which is notably smaller than that of Pt/C (138.72 mV/dec) (Fig. S4 (a)).

Chronocurrent measurements at a constant potential of 0.7 V (Fig. S4(b)) show that Pt/Fe-N-C retains 90% of its initial current after 30000 s, significantly outperforming Pt/C (76%). The mass-specific activity of Pt/Fe-N-C is 276.58 mA/mg at 0.85 V, which is 2.39 times that of Pt/C (Fig. 4(b)).

To evaluate the catalytic selectivity of ORR, hydrogen peroxide (H_2O_2) production and electron transfer during ORR detect were detected using a rotating ring electrode measurement (Fig. 4(c)). The mean electron transfer number (n) and the hydrogen peroxide yield at potentials ranging from 0 to 0.8 V were calculated as 3.99% and 3%, respectively. These results indicate that the four-electron reduction pathway dominates the conversion of O_2 to OH^- during ORR, where oxygen is directly reduced to hydroxide (OH^-) rather than forming hydrogen peroxide (H_2O_2). In contrast, platinum-based alloy catalysts such as PtNP-ZnO@CQDs and Pt-NP/CNR H_2O_2 yields around 20% [45,46], while the Pt/Fe-N-C catalyst synthesized in this study exhibits a significantly lower H_2O_2 yield of only 3%, indicating higher selectivity for the four-electron reduction pathway during the ORR, favoring the direct reduction of oxygen to water (OH^-) rather than the formation of H_2O_2.

In a 0.1 mol/L $HClO_4$ solution, Pt/Fe-N-C achieves an $E_{1/2}$ of 0.85 V, which is superior to Pt/C (0.801 V) (Fig. 4(d)). After 10000 ADT cycles in 0.1 mol/L $HClO_4$ saturated with O_2, the $E_{1/2}$ of Pt/C decreases by 40 mV, while the Pt/Fe-N-C shows no significant shift, indicating superior electrochemical stability during the electrocatalytic ORR process. The mass activity of Pt/Fe-N-C at 0.85 V is 2.11 times that of Pt/C (Fig. 4(e)).

Electrochemical impedance spectroscopy (EIS) was

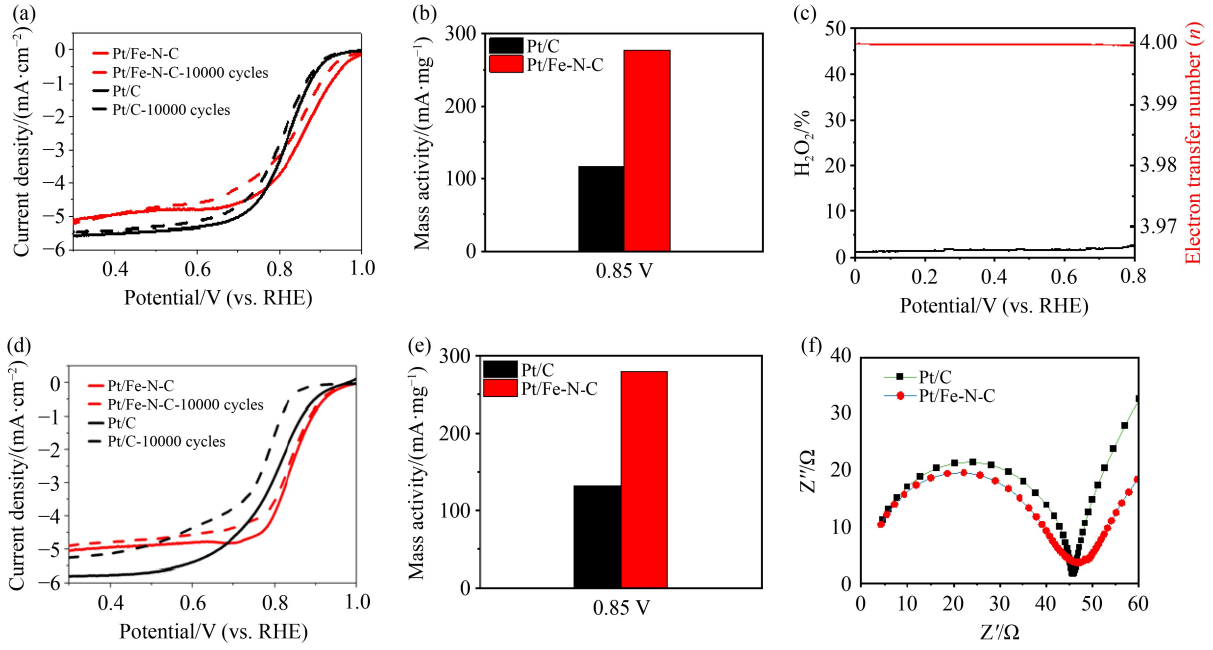

Fig. 4 Electrochemical performance of Pt/Fe-N-C catalysts.

(a) LSV curves and accelerated durability testing of Pt/C, Pt/Fe-N-C in a 0.1 mol/LKOH solution at saturation; (b) comparison of the mass activity of Pt/C and Pt/Fe-N-C in alkaline; (c) RRDE test for Pt/Fe-N-C electron transfer number (n) and hydrogen peroxide yield (H_2O_2%); (d) LSV curves and accelerated durability testing of Pt/C, Pt/Fe-N-C in a 0.1 mol/L$HClO_4$ solution at saturation; (e) comparison of the mass activity of Pt/C and Pt/Fe-N-C in acidity; (f) EIS impedance diagram of Pt/C, Pt/Fe-N-C catalysts.

used to investigate the kinetics of electrode processes and surface phenomena. The AC impedance characteristics of electrochemical systems are analyzed by Nyquist diagram [47–49]. The initial point of the semicircle corresponds to the internal resistance (R_s), and the charge transfer resistance (R_{ct}) is related to the diameter of the semicircle. Compared to commercial Pt/C, the Nyquist plot of Pt/Fe-N-C shows a semicircle with a smaller diameter (Fig. 4(f)), reflecting a lower charge transfer resistance. The ORR mechanism was studied by recording polarization curves at different rotational speeds and applying the Koutecky-Levich (K-L) equation (Fig. S5(a)). The slope is consistent at different potentials, showing a good linear relationship, which reflects the first-order kinetics of the reaction involving saturated dissolved oxygen. In the potential range of 0.22–0.60 V, the electron transfer number (n) per oxygen molecule is approximately 3.8, closely matching the theoretical value of Pt/C (4.0), indicating the predominance of the four-electron process in ORR.

Cyclic voltammetry (CV) was used to detect the double-layer capacitance (C_{dl}) of different samples (Figs. S5(b) and S5(c)). The C_{dl} of Pt/Fe-N-C is 4.01 mF/cm^2, indicating a large catalytic area. The electrochemically active surface area (ECSA) of the catalyst was calculaed from the hydrogen underpotential deposition (HUPD) region of the CV curve in a N_2-saturated electrolyte solution (Fig. S5(d)). The ECSA values for the Pt/C and Pt/Fe-N-C catalysts were 42.93 m^2/g_{Pt} and 73.57 m^2/g_{Pt}, respectively. The ECSA of the Pt/Fe-N-C bimetallic catalyst is significantly higher than that of the Pt/C catalyst, indicating enhanced Pt activity in the alloy catalyst.

The potential of Pt/Fe-N-C for practical applications was evaluated by assembling zinc-air batteries. A zinc-air battery was constructed with Pt/Fe-N-C and Pt/C as the air cathode electrocatalysts, using a Zn plate as the anode (Fig. 5(a)). The open-circuit voltage of the battery with Pt/Fe-N-C as the cathode catalyst was 1.451 V, slightly surpassing the open-circuit voltage of 1.440 V for the battery using Pt/C as the cathode catalyst (Fig. 5(b)).

Figure 5(c) shows the single charge and discharge curve for the Pt/Fe-N-C zinc-air battery. The polarization voltage remains stable between 1.0 and 2.4 V. The maximum power density of the Pt/Fe-N-C catalyst is 200 mW/cm^2, which is significantly higher than the 175 mW/cm^2 of commercial Pt/C (Fig. 5(d)).

The long-term cycle durability of zinc-air batteries, with Pt/Fe-N-C as the cathodic oxygen reduction catalyst, was further studied. For the same catalyst loading of 0.5 mg/cm^2 and a constant current density of 10 mA/cm^2, the Pt/Fe-N-C catalyst has a longer discharge duration of approximately 17 h at constant current discharge, compared to Pt/C (Fig. S6(a)). At different constant current densities (Fig. S6(b)), the discharge time is 30, 17, and 7 at 5, 10, and 20 mA/cm^2, respectively.

To test the stability of the catalyst after long-term use, SEM and XPS analyses were performed on the catalyst

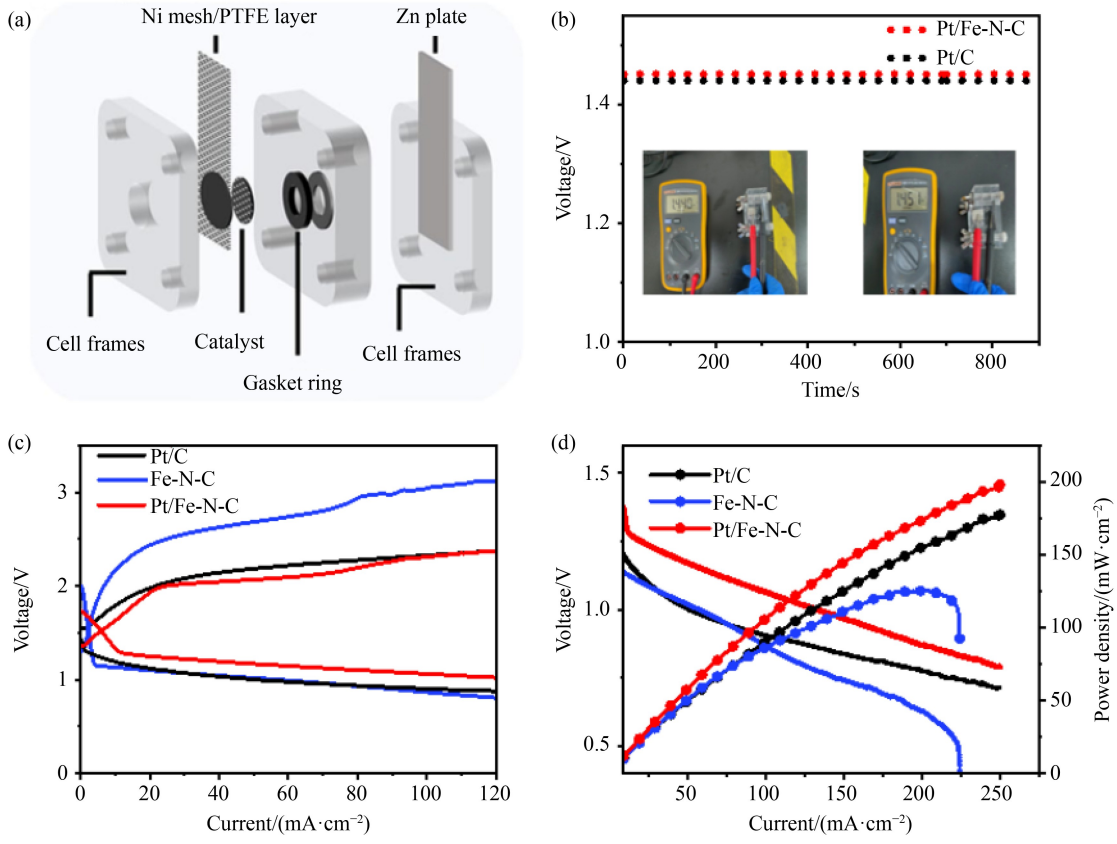

Fig. 5 Performance of Pt/Fe-N-C catalysts in Zn-air battery.
(a) Component diagram of a zinc-air battery; (b) open circuit voltage of Pt/Fe-N-C and Pt/C zinc-air cells; (c, d) power density curve and polarization curve.

after 10000 CV cycles, as shown in Fig. S7. The results showed that the catalyst remained stable even after extensive cycling.

4 Conclusions

This study addresses the challenges of high cost, easy deactivation, and poor durability associated with platinum-based catalysts in the ORR. Initially, a Fe-N-C precursor was synthesized through the PANI pathway. By employing Lewis doping theory and the self-structural constraint effect, the dispersion and exposure of Fe-N-C sites were enhanced. The Fe-N-C sites are homogeneously distributed on the surface of PANI and adsorb platinum ions, leading to the formation of Pt–Fe bimetallic alloys. As a result, an ultra-low Pt loading of just 1.79 wt% was successfully achieved. In terms of catalytic performance, the Pt/Fe-N-C catalyst demonstrates exceptional ORR activity in both acidic and alkaline environments, outperforming commercial Pt/C in terms of mass activity and long-term stability. Moreover, zinc-air batteries assembled with the Pt/Fe-N-C catalyst have achieved a peak power density of up to 200 mW/cm^2. These findings not only validate the catalyst's potential for energy conversion applications but also offer novel insights into optimizing the structure of platinum-based catalysts to enhance their catalytic activity and stability.

Acknowledgements This work was supported by the National Natural Science Foundation of China (Grant No. 22279054).

Competing Interests The authors declare that they have no competing interest.

Electronic Supplementary Material Supplementary material is available in the online version of this article at https://doi.org/10.1007/s11708-025-1006-4 and is accessible for authorized users.

References

1. Chen P, Zhang K, Tang D, et al. Recent progress in electrolytes for Zn-air batteries. Frontiers in Chemistry, 2020, 8: 372
2. Alias M S, Kamarudin S K, Zainoodin A M, et al. Active direct methanol fuel cell: An overview. International Journal of Hydrogen Energy, 2020, 45: 19620–19641
3. Wu D, Shen X, Pan Y, et al. Platinum alloy catalysts for oxygen reduction reaction: Advances, challenges and perspectives. ChemNanoMat: Chemistry of Nanomaterials for Energy, Biology and More, 2020, 6: 32–41

4. Wang Z, Du Z, Wang L, et al. Disordered materials for high-performance lithium-ion batteries: A review. Nano Energy, 2024, 121: 109250
5. Zhu Q, Zhao D, Cheng M, et al. A new view of supercapacitors: integrated supercapacitors. Advanced Energy Materials, 2019, 9(36): 1901081
6. Pan J, Xu Y Y, Yang H, et al. Advanced architectures and relatives of air electrodes in Zn-air batteries. Advanced Science, 2018, 5(4): 1700691
7. Bi X, Jiang Y, Chen R, et al. Rechargeable zinc-air versus lithium-air battery: From fundamental promises toward technological potentials. Advanced Energy Materials, 2024, 14(6): 2302388
8. Liu J N, Zhao C X, Wang J, et al. A brief history of zinc-air batteries: 140 years of epic adventures. Energy & Environmental Science, 2022, 15(11): 4542–4553
9. Ren X, Lv Q, Liu L, et al. Current progress of Pt and Pt-based electrocatalysts used for fuel cells. Sustainable Energy & Fuels, 2020, 4(1): 15–30
10. Jiang Z, Yu J, Huang T, et al. Recent advance on polyaniline or polypyrrole-derived electrocatalysts for oxygen reduction reaction. Polymers, 2018, 10(12): 1397
11. Guo Y, Chen Y N, Cui H, et al. Bifunctional electrocatalysts for rechargeable Zn-air batteries. Chinese Journal of Catalysis, 2019, 40: 1298–1310
12. Liu H, Liu Q, Wang Y, et al. Bifunctional carbon-based cathode catalysts for zinc-air battery: A review. Chinese Chemical Letters, 2022, 33: 683–692
13. Chen J, Dong J, Huo J, et al. Ultrathin Co-N-C layer modified Pt-Co intermetallic nanoparticles leading to a high-performance electrocatalyst toward oxygen reduction and methanol oxidation. Small, 2023, 19(37): 2301337
14. Cruz-Martínez H, Rojas-Chávez H, Matadamas-Ortiz P T, et al. Current progress of Pt-based ORR electrocatalysts for PEMFCs: An integrated view combining theory and experiment. Materials Today Physics, 2021, 19: 100406
15. Hu X, Yang B, Ke S, et al. Review and perspectives of carbon-supported platinum-based catalysts for proton exchange membrane fuel cells. Energy & Fuels, 2023, 37: 11532–11566
16. Hussain S, Erikson H, Kongi N, et al. Oxygen reduction reaction on nanostructured Pt-based electrocatalysts: A review. International Journal of Hydrogen Energy, 2020, 45: 31775–31797
17. Yuan C, Zhang S, Zhang J. Oxygen reduction electrocatalysis: From conventional to single-atomic platinum-based catalysts for proton exchange membrane fuel cells. Frontiers in Energy, 2024, 18: 206–222
18. Chen Y, Zhang S, Chung-Yen Jung J, et al. Carbons as low-platinum catalyst supports and non-noble catalysts for polymer electrolyte fuel cells. Progress in Energy and Combustion Science, 2023, 98: 101101
19. Cai J, Chen J, Chen Y, et al. Engineering carbon semi-tubes supported platinum catalyst for efficient oxygen reduction electrocatalysis. Iscience, 2023, 26(5): 106730
20. Campos-Roldán C A, Parniere A, Donzel N, et al. Influence of the carbon support on the properties of platinum-yttrium nanoalloys for the oxygen reduction reaction. ACS Applied Energy Materials, 2022, 5(3): 3319–3328
21. Ma W, Wu F, Yu P, et al. Carbon support tuned electrocatalytic activity of a single-site metal-organic framework toward the oxygen reduction reaction. Chemical Science, 2021, 12(22): 7908–7917
22. Narasimulu A A, Singh D K, Soin N, et al. A comparative investigation on various platinum nanoparticles decorated carbon supports for oxygen reduction reaction. Current Nanoscience, 2017, 13(2): 136–148
23. Guo S, Dong S, Wang E. Polyaniline/Pt hybrid nanofibers: High-efficiency nanoelectrocatalysts for electrochemical devices. Small, 2009, 5(16): 1869–1876
24. Li C, Zhu L, Song L, et al. Synergistic effect of polyaniline on stabilizing Pt nanoparticles in PEMFCs. Journal of Materials Chemistry. A, Materials for Energy and Sustainability, 2023, 11(14): 7756–7766
25. Li D, Huang J, Kaner R B. Polyaniline nanofibers: A unique polymer nanostructure for versatile applications. Accounts of Chemical Research, 2009, 42(1): 135–145
26. Yin C, Pan C, Pan Y, et al. Proton self-doped polyaniline with high electrochemical activity for aqueous zinc-ion batteries. Small Methods, 2023, 7(11): 2300574
27. Deng H, Li Q, Liu J, et al. Active sites for oxygen reduction reaction on nitrogen-doped carbon nanotubes derived from polyaniline. Carbon, 2017, 112: 219–229
28. Xing S, Yu X, Wang G, et al. Confined polyaniline derived mesoporous carbon for oxygen reduction reaction. European Polymer Journal, 2017, 88: 1–8
29. Hamzehie M E, Samiee L, Fattahi M, et al. Synthesis-structure-performance correlation for poly-aniline-Me-C non-precious metal cathode based on mesoporous carbon catalysts for oxygen reduction reaction in low temperature fuel cells. Renewable Energy, 2015, 77: 558–570
30. Wang Z L, Sun K, Henzie J, et al. Spatially confined assembly of monodisperse ruthenium nanoclusters in a hierarchically ordered carbon electrode for efficient hydrogen evolution. Angewandte Chemie International Edition, 2018, 57(20): 5848–5852
31. Brea C, Hu G. Mechanistic insight into dual-metal-site catalysts for the oxygen reduction reaction. ACS Catalysis, 2023, 13: 4992–4999
32. Lim C, Fairhurst A R, Ransom B J, et al. Role of transition metals in Pt alloy catalysts for the oxygen reduction reaction. ACS Catalysis, 2023, 13: 14874–14893
33. Xiong Y, Yang Y, DiSalvo F J, et al. Synergistic bimetallic metallic organic framework-derived Pt–Co oxygen reduction electrocatalysts. ACS Nano, 2020, 14(10): 13069–13080
34. Wang W, Wang Z, Wang J, et al. Highly active and stable Pt–Pd alloy catalysts synthesized by room-temperature electron reduction for oxygen reduction reaction. Advanced Science, 2017, 4(4): 1600486
35. Liu B, Feng R, Busch M, et al. Synergistic hybrid electrocatalysts of platinum alloy and single-atom platinum for an efficient and durable oxygen reduction reaction. ACS Nano, 2022, 16: 14121–14133
36. Zhou Z, Zhang H J, Feng X, et al. Progress of Pt and iron-group transition metal alloy catalysts with high ORR activity for

PEMFCs. Journal of Electroanalytical Chemistry, 2024: 118165
37. Hu B, Yang Y, Cao W, et al. Patchy Fe-N-C supported low-loading Pt nanoparticles as a highly active cathode for proton exchange membrane fuel cells. Journal of Alloys and Compounds, 2023, 951: 169867
38. Luo B, Zhou F, Pan M. Study on preparation and accessibility of hierarchical porous carbon supported platinum catalyst. Chemical Journal of Chinese Universities, 2022, 43(4): 20210853
39. Shu X, Yang M, Liu M, et al. *In-situ* formation of cobalt phosphide nanoparticles confined in three-dimensional porous carbon for high-performing zinc-air battery and water splitting. Chinese Journal of Catalysis, 2022, 43: 3107–3115
40. Wu Z, Bai J, Lai F, et al. Atomically dispersed platinum supported onto nanoneedle-shaped protonated polyaniline for efficient hydrogen production in acidic water electrolysis. Science China Materials, 2023, 66: 2680–2688
41. Hu K, Xiao X, Du P, et al. Facile fabrication of Mn-N doped porous carbon nanocages with enhanced oxygen reduction reaction activity. Journal of Alloys and Compounds, 2023, 967: 171819
42. Jung W S, Popov B N. Hybrid cathode catalyst with synergistic effect between carbon composite catalyst and Pt for ultra-low Pt loading in PEMFCs. Catalysis Today, 2017, 295: 65–74
43. Song R, Guan L, Fan L, et al. Metal-organic-framework-derived Fe, Co, N-tri-dopped porous carbon as oxygen electrocatalysts for Zn-air batteries. Journal of Energy Storage, 2024, 80: 110345
44. Liu Y, He S, Huang B, et al. Influence of different Fe doping strategies on modulating active sites and oxygen reduction reaction performance of Fe, N-doped carbonaceous catalysts. Journal of Energy Chemistry, 2022, 70: 511–520
45. Pradhan A K, Halder S, Chakraborty C. Pt-nanoparticles on ZnO/carbon quantum dots: A trifunctional nanocomposite with superior electrocatalytic activity boosting direct methanol fuel cells and zinc-air batteries. Journal of Materials Chemistry. A, Materials for Energy and Sustainability, 2024, 13(1): 243–256
46. Pradhan A K, Halder S, Chakraborty C. “Less is more”: Carbon nanostructure-tailored low platinum containing electrocatalysts for improved zinc-air battery efficiency. Journal of Energy Storage, 2024, 98: 113008
47. Han B, Yu S, Wang Z, et al. Imidazole polymerized ionic liquid as a precursor for an iron-nitrogen-doped carbon electrocatalyst used in the oxygen reduction reaction. International Journal of Hydrogen Energy, 2020, 45: 29645–29654
48. Joshi P, Okada T, Miyabayashi K, et al. Evaluation of alkylamine modified Pt nanoparticles as oxygen reduction reaction electrocatalyst for fuel cells via electrochemical impedance spectroscopy. Analytical Chemistry, 2018, 90: 6116–6123
49. Zhang H, Li H, Zhang X, et al. Investigation of phosphoric acid influence on the oxygen reduction reaction on carbon-supported platinum electrocatalyst via rotating disk electrodes. Electrochimica Acta, 2024, 496: 144535